

Insights into Non-adiabatic Flame Temperatures During Millimeter-Size-Vortex/Flame Interactions

V. R. Katta and T. R. Meyer
Innovative Scientific Solutions, Inc.
2766 Indian Ripple Road
Dayton, OH 45440

J. R. Gord and W. M. Roquemore
Air Force Research Laboratory
Propulsion Directorate
Wright-Patterson Air Force Base, OH 45433

Corresponding Author:

Dr. Viswanath R. Katta
Innovative Scientific Solutions, Inc.
2766 Indian Ripple Road
Dayton, OH 45440

Phone: 937-255-8781
Fax: 937-255-3139

Submitted to: *Combustion and Flame*

© 2003. This manuscript version is made available under the CC-BY-NC-ND 4.0 license
<http://creativecommons.org/licenses/by-nc-nd/4.0/>

Insights into Non-adiabatic Flame Temperatures During Millimeter-Size-Vortex/Flame Interactions

V. R. Katta and T. R. Meyer
Innovative Scientific Solutions, Inc.
2766 Indian Ripple Road
Dayton, OH 45440

J. R. Gord and W. M. Roquemore
Air Force Research Laboratory
Propulsion Directorate
Wright-Patterson Air Force Base, OH 45433

ABSTRACT:

Previous experimental and numerical studies have demonstrated that local flame temperatures can significantly increase above or decrease below the adiabatic flame temperature during millimeter-size-vortex/flame interactions. Such large excursions in temperature are not observed in centimeter-size-vortex/flame interactions. To identify the physical mechanisms responsible for these super- or sub-adiabatic flame temperatures, numerical studies have been conducted for millimeter-size-vortex/flame interactions in a hydrogen-air, opposing-jet diffusion flame. Contrary to expectations, preferential diffusion between H_2 and O_2 and geometrical curvature are *not* responsible for these variations in local flame temperature. This was demonstrated through simulations made by forcing the diffusion coefficients of H_2 and O_2 to be equal and, thereby, eliminating preferential diffusion. Propagation of flame into small (~ 1 mm) vortices suggested that the amount of reactant carried by such a small vortex is not sufficient to feed the flame with fresh reactant during the entire vortex/flame interaction process. Various numerical experiments showed that the reactant-limiting characteristics associated with the millimeter-size vortices and the local Lewis number (not preferential diffusion) are responsible for the generation of flame temperature that is different from adiabatic value. The reactant-deficient nature of the millimeter-size vortices forces the combustion products to be entrained into the vortex. While a greater-than-unity Lewis number results in pre-heating of the reactant through the product entrainment, a less-than-unity Lewis number causes cooling of the reactant. Contrary to this behavior, a centimeter-size large vortex wraps and maintains the flame around its outer perimeter by feeding the flame with fresh reactant throughout the interaction process, thereby, rendering the flame unaffected by the Lewis number. Since turbulent flames generally involve interactions with small-size vortices, the physical mechanisms described here should be considered when developing mathematical models for turbulent flames.

NOMENCLATURE:

d_i	Syringe tube diameter
d_o	Nozzle diameter
D_o	Outer nozzle diameter
H	Total enthalpy
H_0	Heat of Formation
K_a	Air-side strain Rate
Le	Lewis number
q	Heat-release rate
r	Radius
R	Radius of curvature
V_f	Flame transitional velocity
t	Time
T	Temperature
T_f	Flame (peak) temperature
T_0	Room temperature
X	Mole fraction
z	Axial distance
ϕ	Equivalence ratio

INTRODUCTION:

Vortex-flame interactions are often considered to be the building blocks for statistical theories of turbulence. During these interactions the flame surface is subjected not only to unsteadiness but also to deformation. To investigate the effects of curvature on unsteady flames, both theoretical and experimental studies have been initiated [1,2]. Experiments designed by Roberts et al., [3] and by Rolon [4] are particularly interesting because of

their unique ability to inject a well-characterized vortex toward the flame surface. Using a counterflow burner similar to that of Rolon, several investigators have studied vortex/flame interactions in which the flame surface is subjected to stretch, deformation, and translation. In general, these studies suggest that 1) moving curved flames can withstand strain rates that are much greater than the corresponding maximum strain rate of a steady planar flame and 2) vortices originating at the air side can quench the flame much easier than those originating at the fuel side. Takagi et al. [5] and Yoshida and Takagi [6] have investigated the effect of curvature on temperature by injecting micro-jets toward the flame surface. Their studies on hydrogen-air diffusion flames revealed that 1) a micro-jet issued from the air side increases the flame temperature at the tip by ~ 300 K and 2) a micro-jet issued from the fuel side decreases the temperature and may cause local extinction. They concluded that this behavior of hydrogen flame is the result of the combined effect of preferential diffusion and flame curvature with respect to the incoming fuel. They argued that the higher diffusivity of hydrogen renders the region at the tip of a concave (negative-curvature) flame fuel rich and that at the tip of a convex (positive-curvature) flame fuel lean. Calculations made for these micro-jet/flame interactions by Yoshida and Takagi [6] and Lee et al. [7] also predicted this behavior. However, insufficient analysis of the results did not validate the conclusions of Takagi et al [5] regarding the effects of preferential diffusion on flames.

Motivated by these observations, Finke and Grunefeld [8] modified the counterflow burner to generate stationary curved flames. Using a 5-mm bluff body embedded in fuel flow or in airflow, they obtained either a concave or convex flame with respect to the incoming fuel. Noting that a concave flame extinguished annularly and that a convex flame extinguished at the center, they also concluded that flame curvature and preferential diffusion are responsible for such flame behavior.

The objective of this study was to employ numerical simulations to gain a better understanding of the physical processes responsible for the observed super- and sub-adiabatic flame temperatures during millimeter-size-vortex/flame interactions. Several investigators have developed models [9-11] for studying vortex-flame interactions in opposing-jet flames. In all of these models, it is assumed that a vortex pair created through the superimposition of a synthesized-vorticity field interacts with a flat flame formed in a parallel flow. Although such an assumption has advantages when exploring interesting aspects of vortex-flame interactions, investigations employing this assumption may not represent actual experimental vortex/flame interactions. Hence, this approach does not facilitate direct comparisons between predictions and experimental results and makes verification of the

former difficult. However, multidimensional models that incorporate detailed chemical kinetics [12,13] are capable of simulating the vortex evolution in an opposing-jet-flow configuration and its interaction with the flame simultaneously.

In the present study simulations of the millimeter-size-vortex/flame interaction were made to demonstrate the ability of the numerical model employed. Computational experiments were then performed to lend insight into the role of preferential diffusion, curvature, strain rate, and Lewis number in generating super- or sub-adiabatic flame temperatures during these vortex/flame interactions.

NUMERICAL MODEL:

Time-dependent, axisymmetric Navier-Stokes equations written in the cylindrical-coordinate (z - r) system are solved along with species- and energy-conservation equations [14]. A detailed-chemical-kinetics model is used to describe the hydrogen-air combustion process. This model consists of thirteen species--namely, H_2 , O_2 , H , O , OH , H_2O , HO_2 , H_2O_2 , N , NO , NO_2 , N_2O , and N_2 . A detailed-chemical-kinetics model having 74 reactions among the constituent species is used; the rate constants for this H_2 - O_2 - N_2 reaction system were obtained from Ref. [15].

Temperature- and species-dependent property calculations are incorporated. The governing equations are integrated on a nonuniform staggered-grid system. An orthogonal grid having rapidly expanding cell sizes in both the axial and radial directions is employed. The finite-difference forms of the momentum equations are obtained using an implicit QUICKEST scheme [16,17] and those of the species and energy equations are obtained using a hybrid scheme of upwind and central differencing. At every time step the pressure field is calculated by solving the pressure Poisson equations simultaneously and utilizing the LU (Lower and Upper diagonal) matrix-decomposition technique. This model, called UNICORN (UNsteady Ignition and COmbustion with Reactions), has been extensively validated [18] by simulating various steady and unsteady counterflow [19] and coflow [14,20] jet diffusion flames and by comparing the results with experimental data.

RESULTS AND DISCUSSION:

Modeling Rolon-Burner Flames:

The opposing-jet-flame burner used for these studies was designed by Rolon [4] and is shown in Fig. 1, along with the experimental and computational results for a millimeter-size-vortex/flame interaction. The burner assembly consists of 25-mm-diameter nozzles (d_o), 40-mm-diameter outer nozzles (D_o), and syringe tubes of 0.2-mm to 5-mm diameter (d_i). A flat flame is formed between the fuel and air jets having velocities of 0.69 and 0.5 m/s, respectively. The hydrogen-to-nitrogen ratio employed for the fuel jet is 0.38. Calculations for the steady-state axisymmetric flame were made using a non-uniform 801 x 336 mesh system distributed over a physical domain of 20 x 20 mm, which yielded a mesh spacing of 0.02 mm in both the axial (z) and the radial (r) directions in the region of interest. The computed air-side strain rate along the stagnation line is 48 s^{-1} . The peak temperature of 1560 K of this weakly strained flame is only slightly lower than the corresponding adiabatic temperature of 1598 K.

Air-Side-Vortex/Flame Interaction:

Vortices are shot toward the flame surface from the air-side by injecting a specified amount of air through the syringe tube (Fig. 1) and then through a 0.2-mm-diameter micro injection tube. Evolution of the injected micro-vortex (initial diameter < 1 mm) and its interaction with the flame surface is dependent on the injection duration. In general, with the shorter injection times, the generated vortices travel faster toward the flame surface and influence the flame structure as the local-flow time scales approach the chemical time scales. A typical experimental image of the millimeter-size-vortex/flame interaction is shown in Fig. 1. This represents the OH concentration field captured using the planar laser-induced fluorescence (PLIF) measurement technique and clearly shows the significant increase in OH concentration in the head region of the vortex. Results obtained from the calculations made for the millimeter-size-vortex/flame interaction in Fig. 1 are shown on the right-hand side of the experimental image. Calculations also predicted the significant increase in the concentration of OH in the head region. The computed OH distribution matches qualitatively the uncorrected experimental OH-PLIF data. The somewhat broad and diffused distribution of OH in the vortex-head region in the experiment could be attributed to the alignment of the laser sheet with the axis of the injection tube. The inner and outer radii of the protrusion of the OH layer that occurred as a result of the vortex penetration are only ~ 0.3 and 0.7 mm, respectively; --of the

order of the laser-sheet thickness (~ 0.4 mm). A small misalignment of the laser sheet with the centerline of the OH protrusion could cause the capture of the OH that is present circumferentially and blur the fluorescence image.

Both in the experiment and the calculations, the interaction between the millimeter-size vortex and the flame resulted in local quenching (hole) of the latter along the stagnation line during the early stages; then the flame was reconnected within 1 ms. The temperature and OH concentration began to increase soon after the reconnection of the extinguished flame (hole), and this increase continued monotonically with time and further propagation of the vortex. Calculations as well as experiments [21] using different injection velocities resulted in very similar interaction sequences; namely, quenching, re-ignition, and an increase in temperature above the adiabatic value in the head region of the vortex.

A detailed view of the millimeter-size-air-vortex/flame interaction at 2.8 ms after the start of air injection is shown in Fig. 2. The structure of the vortex is identified through a plot of the instantaneous locations of the particles that were injected from the air nozzle. The vortex initiated by the 0.2-mm-diameter micro-tube has grown in size to a diameter of 2.9 mm. Instantaneous temperature and H₂O-concentration distributions are plotted in Fig. 2 on the left and right sides, respectively. The temperature of the flame in the head region has increased to 1792 K, which is ~ 194 K higher than the adiabatic flame temperature obtained based on cold reactants. Also, the flame has propagated into the core of the vortex. The instantaneous curvature of this flame is ~ 1.5 mm⁻¹. Earlier calculations [19] made with a 5-mm injection tube that generated a ~ 15 -mm-diameter vortex (shown in Fig. 3) did not reveal this behavior. Even though calculations and the corresponding experiments for this centimeter-size-vortex/flame interaction did not reveal temperatures that are greater than the adiabatic value, a significant amount of curvature (~ 0.14 mm⁻¹) to the flame surface was generated. This indicated that the curvature alone may not be responsible for the increase in temperature observed during the millimeter-size-vortex/flame interactions. Note that the vortex diameter of 15 mm in Fig. 3 is nearly five times larger than the stretched-flame thickness (~ 3 mm, based on the full width of the temperature profile) at the centerline, while the vortex diameter of 3 mm in Fig. 2 is the same as the flame thickness.

In addition to the difference in the flame-thickness-to-vortex-diameter ratios for millimeter-size (Fig. 2) and centimeter-size (Fig. 3) vortex/flame interactions, the structure of these two flames varies significantly. As mentioned earlier, the temperature at the head of the millimeter-size vortex has increased, while that of the

centimeter-size vortex has decreased. The flame in Fig. 2 has penetrated significantly into the vortex and distorted it. On the other hand, the flame in Fig. 3 has remained near the periphery of the vortex. A view along the centerline in Fig. 2 reveals a shift in the distribution of H₂O with respect to the distribution of the temperature, with the peak in the former appearing 0.1 mm downstream of that in the latter. On the other hand, no shift in the locations of the peaks in H₂O and temperature distribution is observed in Fig. 3.

Fuel-Side-Vortex/Flame Interaction:

Calculations were made for the interaction of a millimeter-size fuel-side vortex and the flame using the injection scheme shown in Fig. 1, except that the injector-tube assembly is now placed in the fuel nozzle. The velocity of the injected fuel was chosen to be only 12 m/s, which was significantly lower than that used for the air-side vortex (20 m/s), since the fuel-side millimeter-size-vortex/flame interactions seem to promote local extinction. The instantaneous temperature and OH-concentration distributions simulated 5 ms after the start of fuel injection are shown in Fig. 4 on the left and right sides, respectively. The millimeter-size vortex (~ 3.0-mm diameter) that developed from the injection of fuel is also shown in Fig. 4 via a plot of the instantaneous locations of the particles that were injected from the fuel nozzle. Even this slowly moving vortex extinguished the flame at the center (peak temperature dropped to 720 K) and did not promote to reconnection of the flame hole or temperature buildup. In fact, calculations made with various injection velocities failed to generate a case in which the extinguished flame hole is reconnected while the fuel-side vortex is still traveling through the flame.

Discussion on Super-Adiabatic Flame Temperatures:

Inconsistency in the Existing Theory:

The differences in the interactions of air-side and fuel-side millimeter-size vortices with a diffusion flame were described earlier by Yoshida and Takagi [6] and Lee et al [7]. They attributed these differences to the preferential diffusion among H₂, O₂, and N₂ and the focusing/defocusing nature of the curved flame.

The diffusion coefficient of hydrogen is ~ 3.5 times larger than that of oxygen. Yoshida and Takagi [6] speculated that this difference in diffusion coefficients generates regions with high concentrations of H₂ in the

concave flame (with respect to the fuel), as in Fig. 2, and lower concentrations of H_2 in the convex flame, as in Fig. 4. They used the H_2 ratio (the mole fraction of H_2 in the fuel that should have been available locally prior to combustion) to identify the fuel-rich and fuel-lean regions. This variable estimates the concentration of H_2 from the local product composition. If all of the products are produced locally, then the H_2 ratio exactly yields the amount of H_2 present locally before combustion takes place. However, if the products formed at one location are transported to another through convection and diffusion, then the H_2 ratio computed at the latter location represents not only H_2 that was available there prior to combustion but also part of the H_2 that was available at the former location. The major product in a hydrogen flame is H_2O . Water formed at one location and transported to another would yield higher values of the H_2 ratio and, thereby, erroneously higher concentrations of H_2 in the latter region. A view of the H_2O distribution in Fig. 2 suggests that variation in its concentration generally follows the variation in temperature. The H_2 ratio calculated from this high concentration of H_2O certainly indicates the presence of a greater amount of fuel in the region prior to combustion. However, such interpretation from H_2O is incorrect since an appreciable amount of H_2O was transported from upstream locations to the head of the vortex. The mechanism responsible for this transport of H_2O will be discussed later.

Role of Preferential Diffusion:

In a premixed flame a difference in the diffusion velocities of the reactants can cause an increase or decrease in the reactant concentration in the cusp region, depending on the curvature of the flame with respect to the reactants. On the other hand, since the amount of fuel or oxygen that is able to cross the stoichiometric surface in a diffusion flame is negligible, a diffusion flame is not subjected to the focusing or defocusing effect in the creation of higher- or lower-concentration regions of reactants, respectively. If the fuel flux into the flame zone increases due to some reason (for example, due to injection), then the diffusion flame moves to a new location to achieve a balance with the stoichiometric air flux. To demonstrate that preferential diffusion in conjunction with the flame curvature does not lead to fuel-rich and fuel-lean regions in a diffusion flame, calculations were repeated for the millimeter-size-vortex/diffusion-layer interaction by turning off the chemical reactions associated with the simulation shown in Fig. 2. Results in the form of H_2 -concentration and equivalence-ratio distributions are plotted in Fig. 5 on the left and right sides, respectively. The iso-equivalence contour showing the location of the stoichiometric mixture is plotted with white line. The vortex structure at the same instant is represented with black

dots. Note that the vortex in Fig. 5 is only 1.9 mm in diameter and, thus, has a curvature (1.1 mm^{-1}) for the diffusion layer that is comparable to that of the flame in Fig. 2. The limited growth for the vortex in the non-reacting case (Fig. 5) resulted due to lack of volumetric expansion that was present in the flame simulation (Fig. 2). At room temperature the ratio of H_2 to O_2 diffusion coefficients is 3.66, which is slightly higher than the ratio obtained at 2200 K. Therefore, the cold-flow simulation in Fig. 5 includes preferential diffusion effects that are equal to or greater than those that one would expect in the combusting flow. Figure 5 shows that neither the concentration of H_2 nor the equivalence ratio increased as a result of the combined effect of curvature and high preferential diffusion between H_2 and O_2 . Note that in the absence of chemical reactions the mole fraction of H_2 (X_{H_2}) and the H_2 ratio become identical since concentration of H_2O is zero everywhere. Based on the cold-flow results, one would not expect the H_2 concentration (or H_2 ratio)—and, thus, the flame temperature—to increase in a curved diffusion flame. Therefore, it appears that curvature and preferential diffusion are not responsible for the super-adiabatic flame temperatures shown in Fig. 2.

Roles of Strain Rate and Curvature:

To examine further whether variations in strain rate, curvature, and flame velocity are responsible for the temperature excursions noted in Fig. 2, these variations along with those in temperature are plotted (see Figs. 6 and 7). First, variations of strain rate and temperature along the centerline at several instants are shown in Fig. 6. Since the air-side strain rate [22,23] is often used in describing the structure of a flame influenced by the air-side vortex, only the portions of the strain-rate curves in the neighborhood of the air-side value were plotted in Fig. 6. Flame stretching began at $\sim 1.28 \text{ ms}$ when the air-side strain rate was increased to 2000 s^{-1} . However, this value decreased as the flame underwent the extinction process and the vortex faced increasingly less obstruction from the viscous fluid generated at the flame surface. At $\sim 2.08 \text{ ms}$, re-ignition occurred and the flame temperature and strain rate increased rapidly. After $t = 2.24 \text{ ms}$, the air-side strain rate decreased gradually, while the flame temperature increased beyond the adiabatic value.

Next, the flame temperature, velocity, air-side strain rate, and curvature as functions of time were plotted (see Fig. 7). Since the flame around the vortex is not perfectly circular in shape, the average curvature ($1/R$) of the flame is obtained through integration of the local curvature along the flame surface as follows

$$\frac{1}{R} = \frac{1}{r_{\max}} \int_0^{r_{\max}} \frac{\sin(\theta)}{r} dr = \frac{1}{r_{\max}} \int_0^{r_{\max}} \frac{1}{r \sqrt{1 + (dr/dz)^2}} dr$$

Here, r_{\max} is the radius of the flame where the vortex is largest in diameter and the lower limit of zero for the integral represents the flame at the apex (head of the vortex). The flame surface was identified by tracing the peak temperature location as a function of r . Figure 7 shows that during the vortex/flame-interaction process, the flame temperature at the head of the vortex is increasing while the curvature of the flame is decreasing. Note that the flame curvature decreases as the flame increases in size, while the interacting vortex entrains increasingly more of the surrounding fluid. The relationship between the flame curvature and temperature observed in Fig. 7 does not follow the preferential-diffusion-flame-curvature theory proposed by Takagi et al [5, 6]. The latter suggests that the flame temperature should increase with curvature in the case of air-side vortex/flame interaction. This controversy in theory and predictions suggests that curvature may not be the cause for the observed increase in flame temperature. In fact, the studies of Finke and Grunefeld on steady-state curved flames that employed various inert gases [8] could not establish a relationship between flame curvature and quenching limit.

Figure 7 could also suggest that the decrease in air-side strain rate with time after $t = 2.24$ ms could cause an increase in flame temperature. However, the strain rates ($> 2500 \text{ s}^{-1}$) to which the flame is subjected between 2.1 and 2.8 ms are well above the quenching limit (1770 s^{-1}) [23] and would not yield temperatures that are above adiabatic values; hence, the possibility that the strain rate causes the super-adiabatic flame temperature can be ruled out. Similarly, since the flame is traveling with the vortex, the translational velocity of the former reaches a very high ($\sim 3.5 \text{ m/s}$) value and, hence, its role in causing a diffusion flame to burn intensely can also be ruled out.

Role of Chemical Activity:

Another method of identifying the possibility of increased H_2 concentration generating higher temperature in the tip region is to study the chemical activity in that region. This can be accomplished by calculating the heat-release rate through chemical kinetics. Figure 8 shows the variations of peak temperature and peak heat-release rate along the centerline with time for the air-side millimeter-size-vortex/flame interaction. Various regimes of the interaction process are also indicated in this figure. Note that the peaks in temperature and heat-release rate along the centerline do not necessarily occur at the same location in the flame. A low peak-heat-release rate of 32

$\text{J}/\text{cm}^3/\text{s}$ appears when the flame is in steady state, i.e., before it was affected by the incoming vortex. The flame is stretched and becomes unsteady as the vortex begins to interact with it. The heat-release rate increases during this stretching phase as increasingly more fuel and oxidizer are transported into the flame zone and burned. However, since the chemical kinetics cannot consume all of the increased reactant flow, the flame temperature decreases, falling below the quenching limit by $t \sim 1.59$ ms. In the absence of flame, the heat-release rate rapidly decreased initially and then gradually reached a minimum value of $8 \text{ J}/\text{cm}^3/\text{s}$ by $t = 2.02$ ms. During this no-flame phase, the chemical kinetics among the residual product species was responsible for the release of heat.

Interesting temperature behavior is noted during the no-flame phase. Figure 8 shows that after $t = 1.85$ ms, the temperature began to rise even when the heat-release rate was still decreasing. This indicates that hot products were being brought into the head region of the vortex and increased the temperature. The heat-release rate began to rise after $t = 2.02$ ms as a result of the flame propagation from the sides, and eventually re-ignition took place at $t = 2.08$ ms. Because of the premixing between the fuel and air that occurred in the absence of the flame, a spike in the peak heat-release rate was established during the re-ignition process. Note that the peak heat-release rate following the spike ($\sim 600 \text{ J}/\text{cm}^3/\text{s}$) did not reach the value experienced by this flame prior to extinction, even though the stretch on the flame had increased to a value ($\sim 3300 \text{ s}^{-1}$) that was much higher than the peak strain rate ($\sim 2000 \text{ s}^{-1}$) imposed on the flame prior to extinction (cf. Fig. 6). Typically, the heat-release rate in a *pure* diffusion flame increases with strain rate as reactant fluxes increase with strain rate. The failure to generate a higher heat-release rate in the diffusion flame in Fig. 6 after the re-ignition suggests that the strain rate, in fact, did not produce higher reactant fluxes—which, may occur if the reactant in the vortex is partially depleted.

Figure 8 also shows that during the vortex-propagation stage ($t > 2.24$ ms) while the heat release rate was decreasing, the temperature continued to increase. This behavior suggests that the reactant fluxes (H_2 and O_2) into the flame zone are decreasing and, in turn, the heat-release rate. Therefore, the increase in flame temperature for $t > 2.24$ ms is due neither to an increase in chemical activity nor to an increase in H_2 mole fraction, as was suggested previously [5,6].

Role of Lewis Number:

To gain insight into the origin of the super-adiabatic flame temperature, numerical experiments were performed where certain physical or chemical processes were turned off. Figure 9 shows the air-side millimeter-size-

vortex/flame interaction simulated by forcing the Lewis number to unity. Lewis number (Le) is defined as the ratio between the heat and mass transport. In a multicomponent mixture, one should expect several Lewis numbers—each one corresponds to a specific species in the mixture. Therefore, the diffusion coefficient of every species is made equal to that of hydrogen while forcing the heat-transfer rate to be equal to the mass-diffusion rate to achieve the unity-Lewis-number condition in the multi-component mixture. Because of this higher diffusion coefficient, the flame became thicker than the normal one shown in Figs. 2-4. Note that the chemical kinetics was not altered in this simulation. The temperature of the stationary flame decreased to 1400 K with the unity-Lewis-number assumption. This results from the flame shifting to the fuel side of the stagnation plane where the N_2 concentration is higher (nearer to that in the fuel stream). Figure 9 shows that the temperature near the tip of the millimeter-size vortex is ~ 50 K above the stationary flame temperature. Although this increase in temperature in unity-Lewis-number simulation is not so high as that observed in Fig. 2, the result does suggest that preferential diffusion among species is not important in explaining the super-adiabatic flame temperatures. The role of non-unity Lewis number in increasing temperature by 194 K in Fig. 2 is examined later.

Unity-Lewis-number calculations made by setting the diffusion coefficients of all the species equal to that of oxygen also yielded similar excursions in temperature during the interactions between the air-side millimeter-size vortex and the flame. Furthermore, a unity-Lewis-number calculation was also made for the fuel side millimeter-size-vortex/flame interaction described in Fig. 4. This simulation also resulted in an increase in flame temperature similar to that observed with an air-side vortex. For the calculation shown in Fig. 4, the Lewis number is actually lower than one, and the flame was quenched. These simulations with the unity-Lewis-number assumption suggest that the Lewis number contributes to the super- and sub-adiabatic flame temperatures observed during millimeter-size-vortex/flame interactions. However, in earlier studies [19] on interactions of larger vortices with the same flame, excursions in flame temperature did not result. This suggests that some characteristics of millimeter-size vortices in conjunction with non-unity Lewis number are responsible for the super- and sub-adiabatic flame temperatures noted in Figs. 2 and 4. The question remains concerning which characteristic associated with vortex size contributes to the temperature changes.

Impact of Limited Supply of Reactants:

Re-examination of the vortex and flame structures associated with the millimeter-size-vortex/flame (Figs. 2 and 9) and the centimeter-size-vortex/flame (Fig. 3) [19,23] interactions brought to light a unique feature associated with the former. During the centimeter-size-vortex/flame interaction, the flame always remains near the head of the vortex. This suggests that the vortex contains an abundant quantity of reactant. Also, during this interaction, the vortex always transports cold reactant into the flame. However, when the vortex is small, the flame moves into the vortex. This suggests that the diffusion flame is depleting the reactant contained within the millimeter-size vortex, consistent with the heat-release-rate data presented in Fig. 8. This case represents a reactant-limited interaction. As the reactant mass is depleted, the vortex transports products (which include product species and heat) along with the remaining reactant into the flame. The flame temperature depends on the composition of fluid that is transported into the flame by the vortex. For example, if the vortex transports heated mass into the flame, then one should expect an increase in flame temperature. If it transports cold products (water gas), then a decrease in flame temperature should occur. The composition of the products generated in a diffusion flame depends on how the reactants and heat are transported in and out, respectively; i.e., on the local Lewis number.

Lewis Number and Reactant-Limitedness in Jet Flames:

To explain the role of the Lewis number and the characteristics associated with the millimeter-size vortices in altering the flame temperature, a simple case that eliminates unsteady, non-equilibrium chemistry and non-uniform transport properties was selected. Numerical simulations for an axisymmetric, reactant-limited jet flame were performed using constant properties and Lewis number and infinitely fast global-reaction assumptions. Calculations made for a jet flame with either fuel or air inside yielded identical results. The temperature and H₂O concentration fields obtained for three steady-state flames having different Lewis numbers are shown in Fig. 10 for the fuel-inside-flame case. The velocity of the fuel and air jets is 0.2 m/s, which yielded complete burning of the fuel within a 130-mm height. Calculations made with higher velocities and larger fuel-tube diameters yielded perfectly straight flames, with no change in flame temperature with height. The normalized temperature and H₂O concentration distributions at a height of 50 mm above the inlet for the three flames are compared in Fig. 11.

Two important points must be highlighted in the results shown in Fig. 10. First, the flames are fuel-limited and, therefore, converge toward the axis of symmetry. Second, the water concentration is always highest at the flame

tip. This is due to the cumulative process of water formation in the flame (H_2O in these flames has an infinite lifetime). When $Le = 1$ [Fig. 10(a)], the flame temperature increases with height and reaches a peak value at the tip—consistent with the unity-Lewis-number simulation made for the air-side millimeter-size-vortex/flame interaction in [Fig. 9]. The reason for this behavior becomes clear when the temperature and H_2O distributions in Fig. 10(a) are compared. By definition, in the case of $Le = 1$, both product (H_2O) and heat diffuse similarly. However, Fig. 10(a) suggests that the temperature is diffusing faster than the H_2O (distribution of temperature is wider at the center compared to that of H_2O). The reason for such behavior in $Le = 1$ diffusion flames will now be discussed.

When the Lewis number is equal to unity, heat and mass diffuse similarly provided that the gradients for heat and mass are also the same. The reason for this is that the diffusive flux is the product of the diffusion coefficient and the mass (or enthalpy) gradient. It is known that the specific heat of water is significantly higher than that of either H_2 or O_2 . Thus, at room temperature, the enthalpy ($H - H^0$) of H_2O will be higher than that of H_2 or O_2 . The enthalpy gradient between H_2O in the flame zone and cold reactants away from the flame would be the same as the mass gradient for the generated H_2O if and only if the enthalpy of the cold reactants is the same as that of cold H_2O . Because of the difference in specific heats, the enthalpy of H_2 or O_2 is lower than that of cold (room temperature) H_2O . As a result, the enthalpy (or temperature) gradient is greater than the mass gradient. This higher enthalpy gradient produces higher heat flux and, thus, more diffusion of heat than of mass, even when the Lewis number is unity. This results in preheating of the reactants. Since specific heats of both H_2 and air are lower than that of H_2O , this preheating should occur on both sides of the diffusion flame, no matter which reactant is at the center, as is evident in Fig. 11. The temperature profile for the $Le = 1$ flame is more diffused on both sides of the flame than the H_2O distribution. In a perfectly flat flame, both reactants are in abundance and the preheated reactants do not enter the flame zone to raise the flame temperature, which results in a self-similar solution. However, if these preheated reactants enter the flame at downstream locations, the temperature of the flame can increase beyond the adiabatic value. This can happen when one of the reactants is deficient. Flames naturally curve toward the deficient reactant at downstream locations. As seen in Fig. 10(a), the preheating of the deficient reactant (fuel) at the center has caused the temperature to increase at the tip of the flame.

When the $Le = 0.5$, heat diffuses much more slowly than the products (H_2O), resulting in more H_2O at the axis of symmetry [Fig. 10(b)]. The water that diffuses beyond the heat acts as a diluent to the fuel since it is not

transporting heat with it. In fuel-limited flames, such as in Fig. 10, this diluted fuel enters the flame at downstream locations and cools the flame. Because of the accumulation effect, the flame tip is the coldest flame region. On the other hand, when $Le = 2.0$, heat diffuses faster than the products (H_2O) and preheats the fuel at the center. Again, in a fuel-limited flame, this heated fuel eventually enters the flame at downstream locations, making the flame hotter. Because of the accumulation effect, the flame tip is the hottest flame region.

In a hydrogen-air diffusion flame, the Lewis number on the fuel side is near 0.5 and that on the air side is slightly above unity. The amount of fuel or air contained in a millimeter-size vortex or jet is quite small, and the protruded flame becomes reactant-limited. Because of these combined effects, the temperature at the tip of the air-side millimeter-size-vortex/flame interaction increases (Le is slightly greater than unity, and the flame is air-limited), as seen in Fig. 2. The temperature at the head of the fuel-side millimeter-size-vortex/flame interaction decreases ($Le \sim 0.5$ and the flame is fuel limited) as seen in Fig. 4. Even though the Lewis number is greater or smaller than unity in the case of centimeter-size-vortex/flame interactions, the protruded flame contains sufficient reactant; thus, the flame temperature does not change as a result of the non-unity Lewis number. It may decrease because of strain, but it does not increase. Geometrical curvature ($1/R$) does not impact these diffusion flames. Only curvature resulting from reactant deficiency plays a role in altering the flame temperature. To further verify this hypothesis, a calculation for a millimeter-size-air-vortex/flame interaction in a planar two-dimensional flow was performed. Consistent with the above arguments, the flame was significantly curved, but the temperature did not increase at the tip, since the planar vortex contained more air and the protruded flame did not become air-limited.

CONCLUSIONS:

Vortex/flame interactions are often studied to gain an understanding of complex, turbulent reaction processes. A millimeter-size vortex shot toward a flame, generates a protruded flame very similar to the flame bump observed on a turbulent flame. Earlier studies of millimeter-size-vortex/flame interactions suggested that when the vortex originates on the air side, it can increase the flame temperature above the adiabatic value by as much as 300 K. Even though the consequences of these interactions are significant and play a major role in describing a turbulent flame, the exact cause of such variations in flame temperature is not well understood. In the present study, a well-

tested CFD model was used to investigate millimeter-size-vortex/flame interactions. Calculations performed for the air-side and fuel-side millimeter-size-vortex/flame interactions resulted an increase and decrease in flame temperature, respectively. These results qualitatively agree with the experiments and the simulations of Takagi et al [6] and Lee et al [7]. Numerical experiments were performed to identify the physical mechanisms responsible for generating these super-and sub-adiabatic flame temperatures. The results indicated that the geometrical curvature of the flame and preferential diffusion between H_2 and O_2 are not responsible for the super-adiabatic flame temperature. Based on studies conducted using vortices of different sizes and various Lewis numbers and changing the origin of the vortices, the following conclusions have been derived;

- 1) Both the millimeter- and centimeter-size-vortex-flame interactions generate curvature to the flame surface. Preferential diffusion or curvature in a diffusion flame does not cause an increase or decrease in the flame temperature.
- 2) It is known that less-than-unity Lewis number renders a diffusion flame (whether curved or not) hotter and a greater-than-unity Lewis number renders it cooler compared to the similarly stretched unity-Lewis-number flame.
- 3) A centimeter-size vortex possesses reactant in abundance and, hence, its interaction with a diffusion flame could be described by the changes in air-side strain rate. Consequently, the flame temperature decreases as the flame is stretched by the vortex, irrespective of its origin (fuel or air side) or curvature.
- 4) During its interaction with a diffusion flame, a millimeter-size vortex becomes reactant-limited and promotes entrainment of combustion products into the vortex. The heat content of the entrained products (mostly water gas in hydrogen flames) depends on the local Lewis number. If the Lewis number is less than unity, then the vortex entrains cold products and renders the flame cooler. Similarly, if the Lewis number is greater than unity, then the vortex entrains hot (pre-heated) products and renders the flame hotter.
- 5) Geometrical curvature generated during the vortex/flame interactions has no significance in diffusion flames. It becomes important only when the reactant contained in the vortex becomes insufficient during the interaction process. Naturally, the higher the curvature, the more rapidly the vortex becomes reactant-limited.

Although this study was conducted with hydrogen fuel, it is felt that the results are applicable to hydrocarbon diffusion flames also.

ACKNOWLEDGMENTS:

This work was supported, in part, by Air Force Contract F33615-00-C-2068 and the Air Force Office of Scientific Research. The experimental image shown in Fig. 1 was obtained at the Air Force Research Laboratory by Drs. P. H. Renard, J. C. Rolon, and G. J. Fiechtner under a Joint US-French Collaborative Program. The authors would like to thank Marian Whitaker for editorial help

REFERENCES:

1. Paul, P. H., and Najm, H. N., in *Twenty-seventh Symposium (International) on Combustion*, The Combustion Institute, Pittsburgh, PA, 1998, p. 43.
2. Patnaik, G., and Kailasanath, K., in *Twenty-seventh Symposium (International) on Combustion*, The Combustion Institute, Pittsburgh, PA, 1998, p. 711.
3. Roberts, W. L., Driscoll, J. F., Drake, M. C., Ratcliffe, J. W., in *Twenty-fourth Symposium (International) on Combustion*, The Combustion Institute, Pittsburgh, PA, 1992, p. 169.
4. Rolon, J. C., Aguerre, F., and Candel, S., *Combust. Flame* 100:422 (1995)
5. Takagi, T., Yoshikawa, Y., Yoshida, K., Komiyama, M., and Kinoshita, S., in *Twenty-sixth Symposium (International) on Combustion*, The Combustion Institute, Pittsburgh, PA, 1996, p. 1101.
6. Yoshida, K., and Takagi, T., in *Twenty-seventh Symposium (International) on Combustion*, The Combustion Institute, Pittsburgh, PA, 1998, p. 685.
7. Lee, J. C., Frozakis, C. E., and Boulouchos, K., "Numerical Study of an Opposed-Jet H₂-Air Diffusion Flame-Vortex Interactions," Seventeenth International Colloquium on the Dynamics of Explosions and Reactive Systems (ICDERS), Heidelberg, Germany, July 25-30, 1999.
8. Finke, H., and Grunefeld, G., *Proc. Combust. Inst.* 28:2133-2140 (2000).
9. Ashurst, W. T., *Combust. Sci. Technol.* 92:87 (1993).
10. Poinot, T., Trouve, A., Veynante, D., Candel, S., and Esposito, E., *J. Fluid Mech.* 177:265 (1987).
11. Rutland, C. J., and Ferziger, J. H., *Combust. Flame* 84:343 (1991).
12. Smooke, M. D., Ern, A., Tanoff, M. A., Valdati, B. A., Mohammed, R. K., Marran, D. F., Long, M. B., in *Twenty-sixth Symposium (International) on Combustion*, The Combustion Institute, Pittsburgh, PA, 1996, p. 2161.
13. Katta, V. R., and Roquemore, W. M., AIAA Paper 97-0904, Aerospace Sciences Meeting, Reno, NV, Jan., 1997.
14. Katta, V. R., and Roquemore, W. M., *Combust. Flame* 100:61 (1995).

15. Frenklach, M., Wang, H., Goldenberg, M., Smith, G. P., Golden, D. M., Bowman, C. T., Hanson, R. K., Gardiner, W. C., V. Lissianski, V., Gas Research Institute Technical Report No. GRI-95/0058 (Gas Research Institute, Chicago, IL, November 1, 1995).
16. Leonard, B. P., *Comput. Meth. Appl. Mech. Eng.* 19:59 (1979).
17. Katta, V. R., Goss, L. P., and Roquemore, W. M., *AIAA J.* 32:84 (1994).
18. Roquemore W. M., and Katta, V. R., *J. Visualization*, 2:257 (2000).
19. Katta, V. R., Carter, C. D., Fiechtner, G. J., Roquemore, W. M., Gord, J. R., and Rolon, J. C., in *Twenty-seventh Symposium (International) on Combustion*, The Combustion Institute, Pittsburgh, PA, 1998, p. 98.
20. Grisch, F., Attal-Tretout, B., Bouchardy, P., Katta, V. R., and Roquemore, W. M., *J. Nonlin. Opt. Phys. Mater.*, 5:505 (1996)
21. Renard, P. H., Thevenin, D., Rolon, J. C., and Candel, S., *Prog. Energy Combust. Sci.* 26:225-282 (2000).
22. Chelliah, H. K., Law, C. K., Ueda, T., Smooke, M. D., and Williams, F. A., in *Twenty-third Symposium (International) on Combustion*, The Combustion Institute, Pittsburgh, PA, 1990, p. 503.
23. Katta, V. R., and Roquemore, W. M., *Proc. Combust. Inst.* 28:2055-2062 (2000).

LIST OF FIGURES:

Fig. 1. Schematic diagram of opposing-jet burner used in studies of vortex-flame interactions. Inserted images (measured and computed on left and right halves, respectively) are those of typical protruded flame obtained with millimeter-size air-side vortex, showing increase in concentration of OH at tip.

Fig. 2. Structure of flame computed during interaction with millimeter-size air-side vortex. Temperature ($T_{\min} = 294 \text{ K}$ and $T_{\max} = 1800 \text{ K}$) and H_2O concentration ($X_{\text{H}_2\text{O}}|_{\min} = 0$ and $X_{\text{H}_2\text{O}}|_{\max} = 22.8\%$) plotted on the left and right halves, respectively. Linear-rainbow color scale is used to represent various contour levels. Instantaneous locations of particles injected from air nozzle are superimposed.

Fig. 3. Structure of flame computed during interaction with centimeter-size air-side vortex. Temperature ($T_{\min} = 294 \text{ K}$ and $T_{\max} = 1600 \text{ K}$) and H_2O concentration ($X_{\text{H}_2\text{O}}|_{\min} = 0$ and $X_{\text{H}_2\text{O}}|_{\max} = 20.0\%$) plotted on the left and right halves, respectively. Linear-rainbow color scale is used to represent various contour levels. Instantaneous locations of particles injected from air nozzle are superimposed.

Fig. 4. Structure of flame computed during interaction with millimeter-size fuel-side vortex. Temperature ($T_{\min} = 294 \text{ K}$ and $T_{\max} = 1600 \text{ K}$) and OH concentration ($X_{\text{OH}}|_{\min} = 0$ and $X_{\text{OH}}|_{\max} = 0.41\%$) plotted on left and right halves, respectively. Linear-rainbow color scale is used to represent various contour levels. Instantaneous locations of the particles injected from fuel nozzle are superimposed.

Fig. 5. Mixing between fuel (H_2) and oxygen during propagation of millimeter-size air-side vortex. Concentrations of H_2 ($X_{\text{H}_2}|_{\min} = 0$ and $X_{\text{H}_2}|_{\max} = 27.4\%$) and equivalence ratio ($\phi|_{\min} = 0$ and $\phi|_{\max} = 10.0$) plotted on left and right halves, respectively. Linear-rainbow color scale is used to represent various contour levels. White contour line represents stoichiometric-mixture location. Instantaneous locations of particles injected from air nozzle are superimposed.

Fig. 6. Temperature profiles (broken lines) and corresponding applied air-side strain rates (solid lines) along the centerline at different instants during interaction process between millimeter-size air-side vortex and the flame. Times are with respect to start of issuance of air-side vortex.

Fig. 7. Variations of centerline flame (peak) temperature (T_f), air-side strain rate (K_a), flame translational velocity (V_f), and flame curvature ($1/R$) with time during air-side millimeter-size-vortex/flame interaction.

Fig. 8. Peak heat-release rate (q_{max}) and flame temperature (T_f) at different times during air-side millimeter-size-vortex/flame interaction process.

Fig. 9. Structure of flame computed using unity-Lewis-number assumption during interaction with millimeter-size air-side vortex. Temperature ($T_{min} = 294$ K and $T_{max} = 1410$ K) and H_2O concentration ($X_{H_2O}|_{min} = 0$ and $X_{H_2O}|_{max} = 16.2\%$) plotted on left and right halves, respectively. Linear-rainbow color scale is used to represent various contour levels. Regions where temperature is in excess of 1410 K shown in white. Instantaneous locations of particles injected from both air and fuel nozzles are superimposed.

Fig. 10. Steady-state flames calculated using different Lewis-number assumptions. Fuel (H_2) jet is located at center (i.e., inside flame). Temperature and H_2O concentration are plotted on left and right halves, respectively, in each case. Linear-rainbow color scale is used between the minimum and maximum values to represent various contour levels.

Fig. 11. Normalized temperature and H_2O distributions across flame at axial height of 50 mm above inlet for flames obtained with different Lewis-number assumptions.

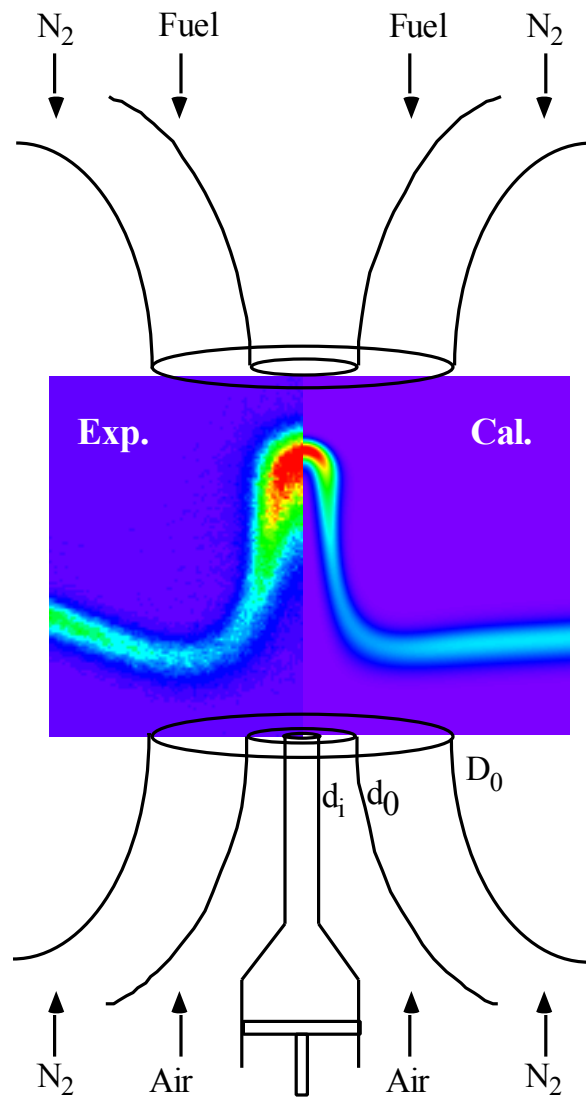


Fig. 1. Schematic diagram of opposing-jet burner used in the studies of vortex-flame interactions. Inserted images (measured and computed on the left and right halves, respectively) are that of a typical protruded flame obtained with a millimeter-size airside vortex showing an increase in the concentration of OH at the tip.

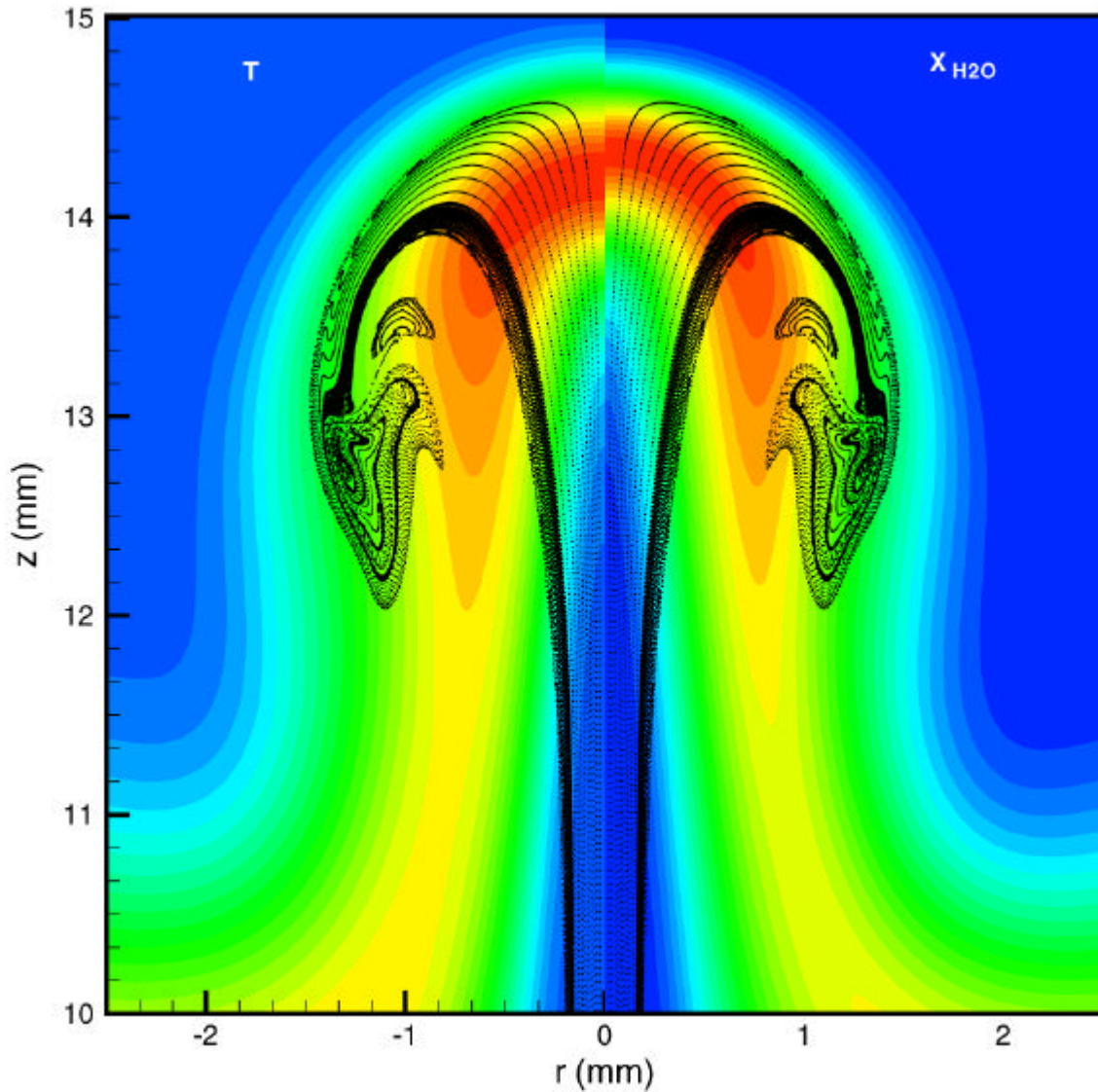


Fig. 2. Structure of the flame computed during its interaction with a millimeter-size airside vortex. Temperature ($T_{\max} = 1800$ K) and H_2O concentration ($X_{H_2O}|_{\max} = 22.8\%$) are plotted on the left and right halves, respectively. The instantaneous locations of the particles injected from air nozzle are superimposed.

Katta et al.

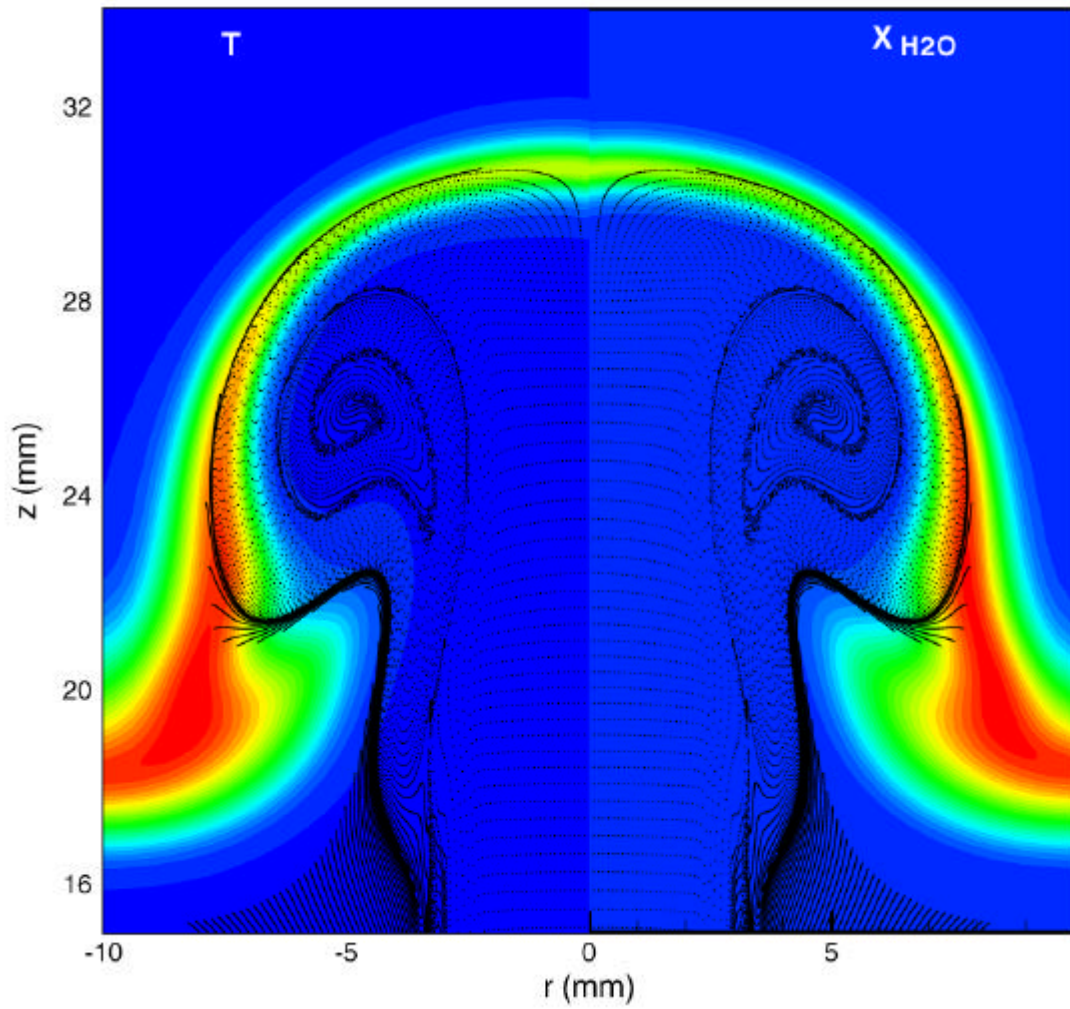


Fig. 3. Structure of the flame computed during its interaction with a centimeter-size-airside vortex. Temperature ($T_{\max} = 1600$ K) and H_2O concentration ($X_{H_2O}|_{\max} = 20.0\%$) are plotted on the left and right halves, respectively. The instantaneous locations of the particles injected from air nozzle are superimposed.

Katta et al.

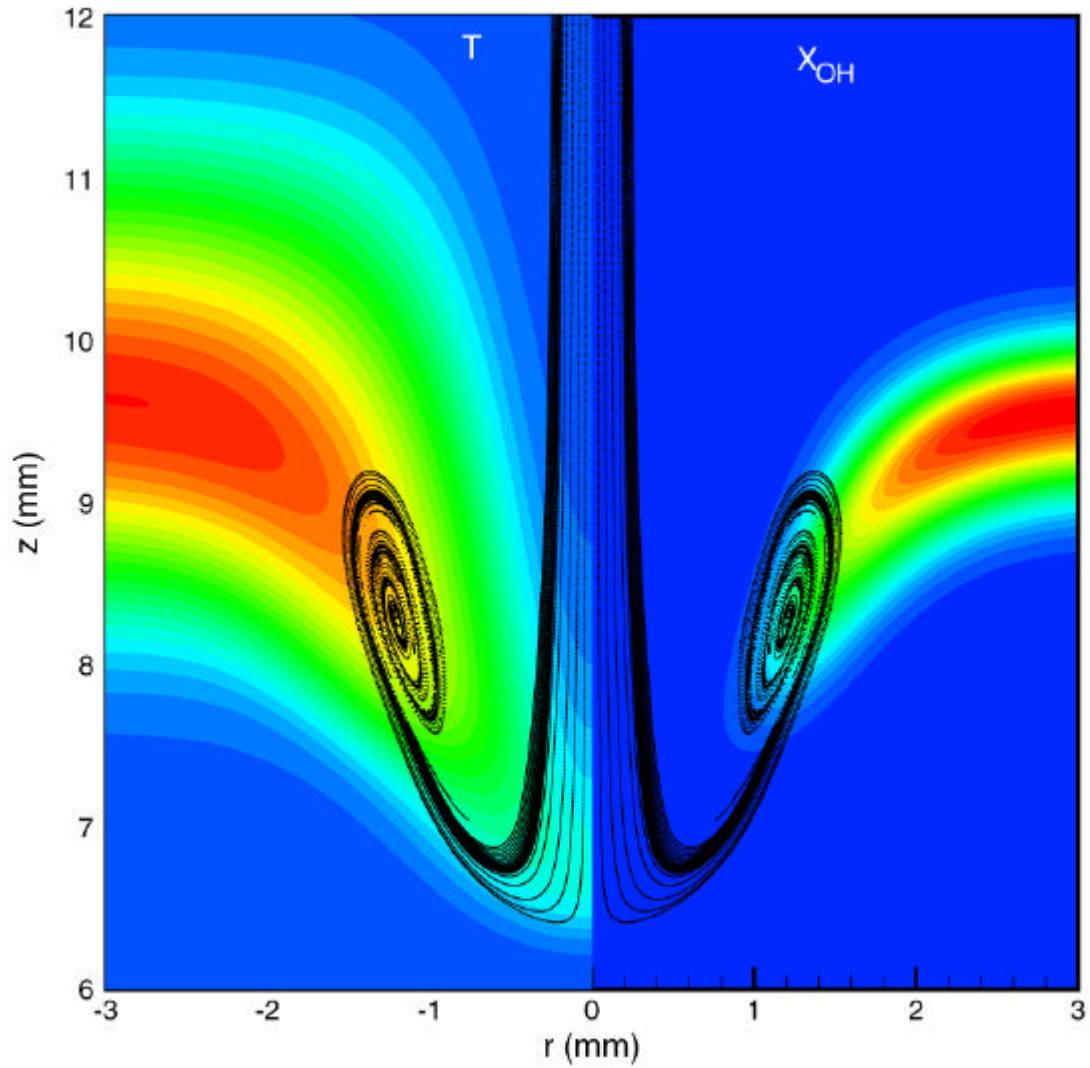


Fig. 4. Structure of the flame computed during its interaction with a millimeter-size fuel-side vortex. Temperature ($T_{\max} = 1600$ K) and OH concentration ($X_{\text{OH}}|_{\max} = 0.41\%$) are plotted on the left and right halves, respectively. The instantaneous locations of the particles injected from fuel nozzle are superimposed.

Katta et al.

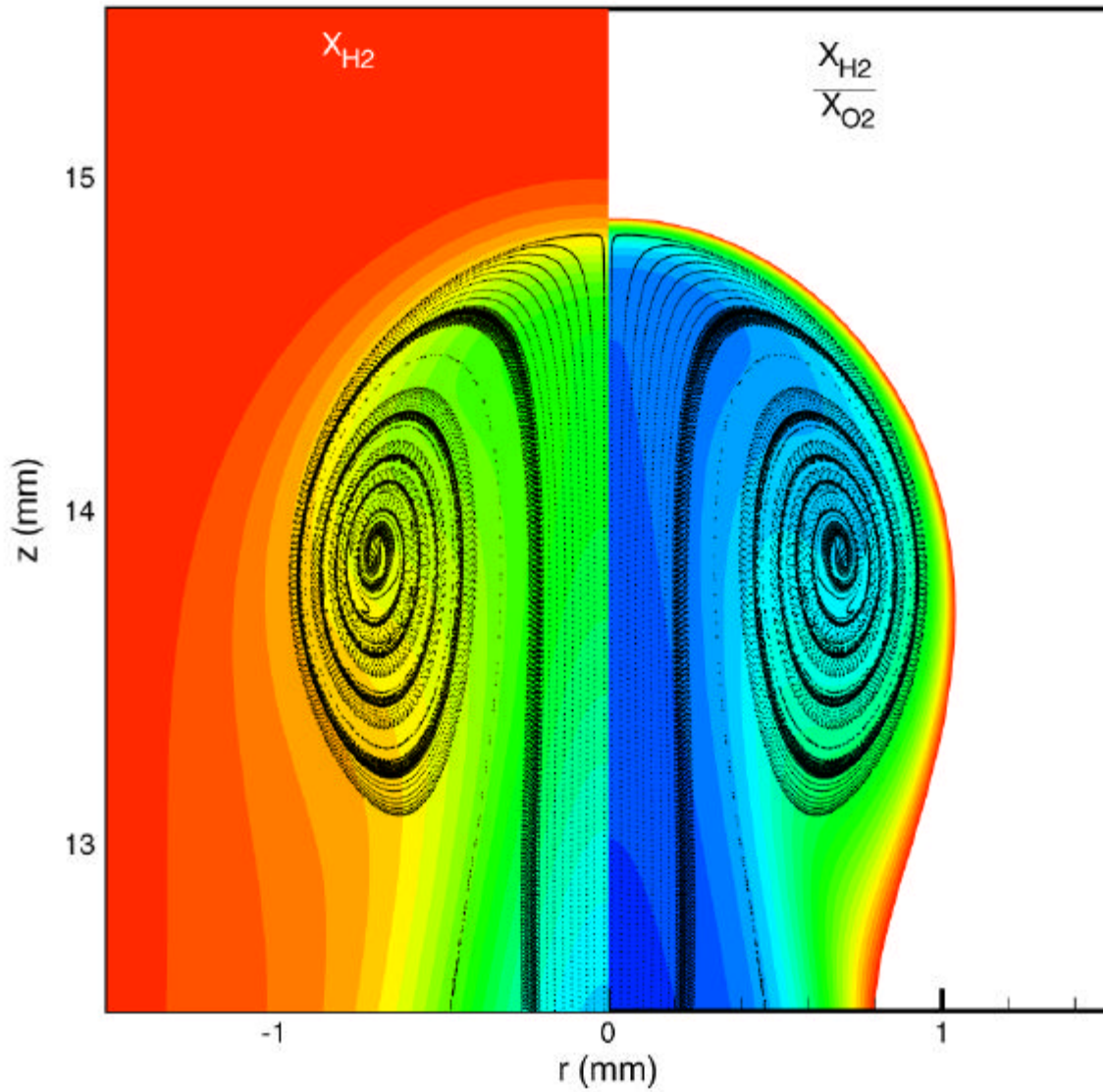


Fig. 5. Mixing between fuel (H_2) and oxygen during the propagation of a millimeter-size airside vortex. Concentrations of H_2 ($X_{H_2}|_{\max} = 27.4\%$) and fuel-oxygen ratio ($?|_{\max} = 10.0$) are plotted on the left and right halves, respectively. The instantaneous locations of the particles injected from air nozzle are superimposed.

Katta et al.

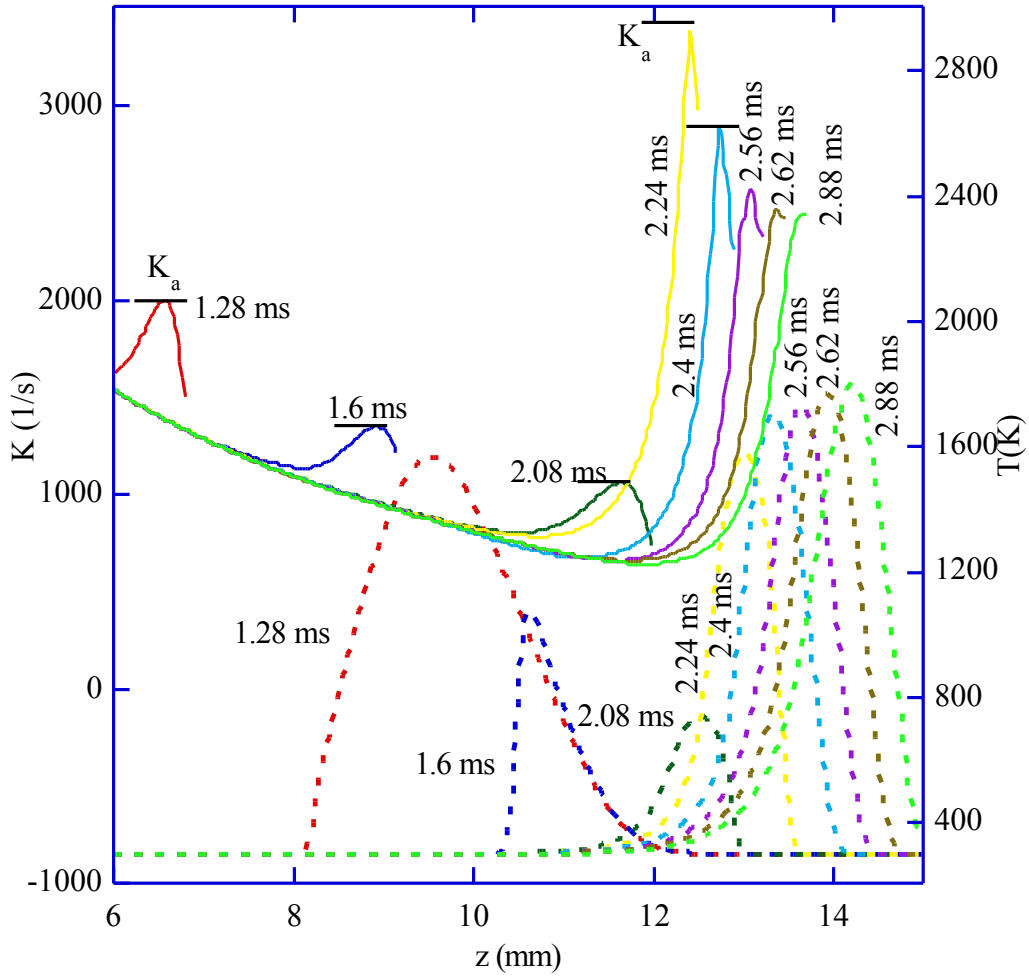


Fig. 6. Temperature profiles and corresponding applied airside strain rates at different instants during the interaction process between a millimeter-size airside vortex and the flame. Here, times are referred with respect to the start of the issuance of the airside vortex.

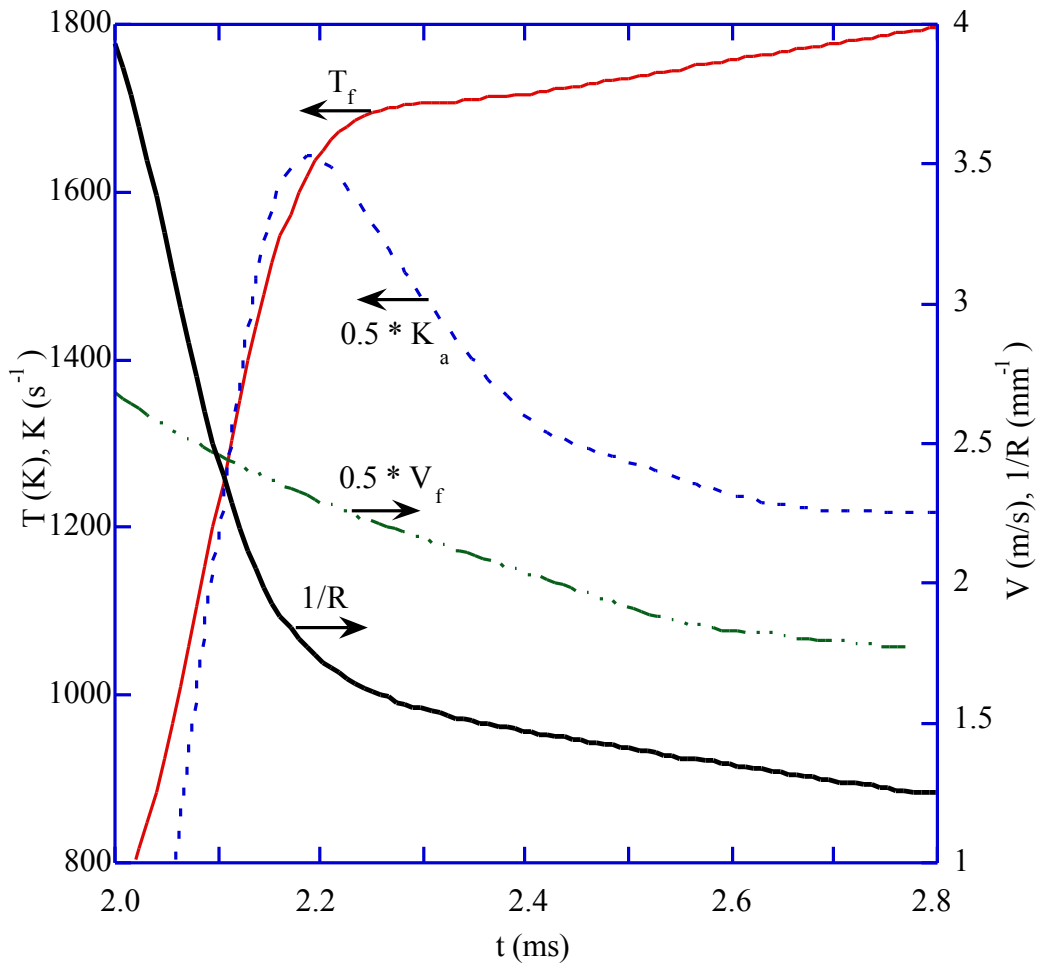


Fig. 7. Variations of flame temperature (T_f), airside strain rate (K_a), flame velocity (V_f), and flame curvature ($1/R$) with time during the airside millimeter-size-vortex/flame interaction.

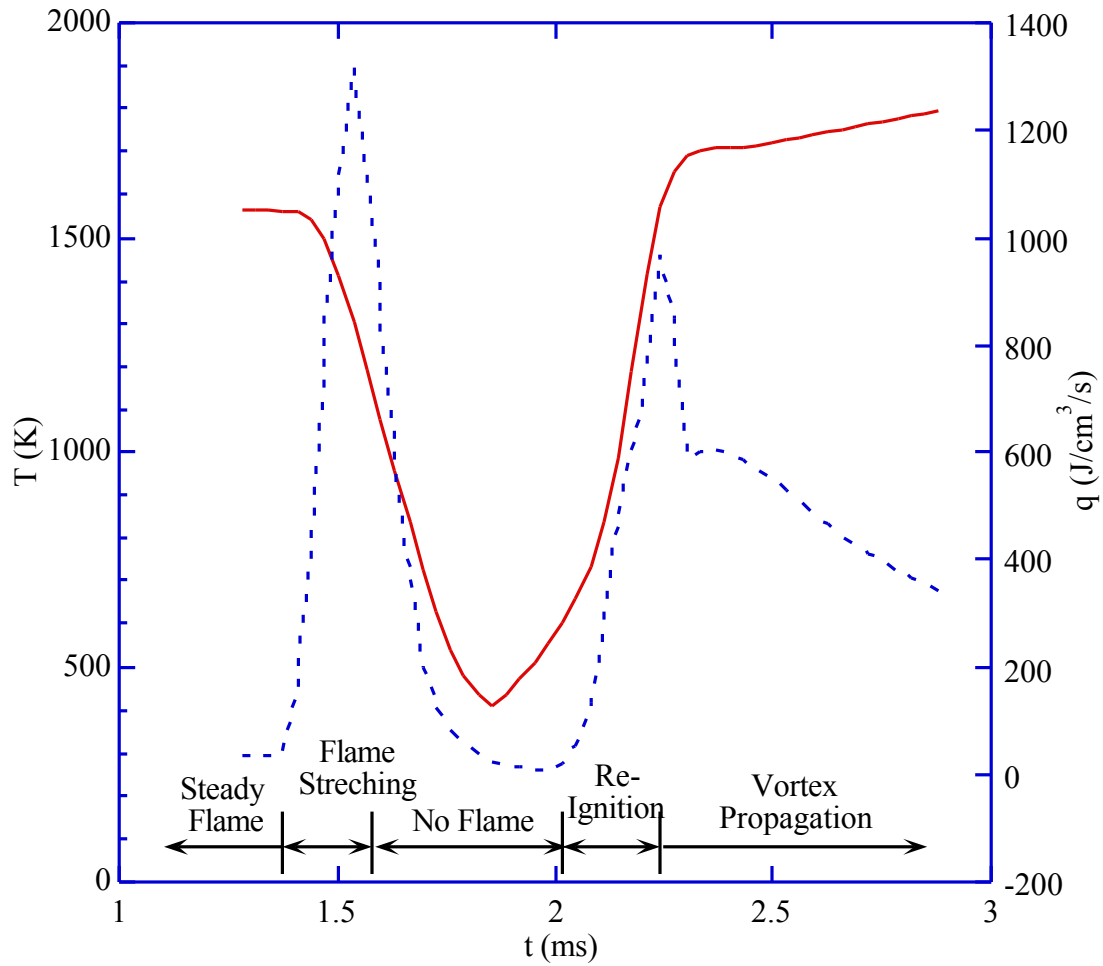


Fig. 8. Peak heat release rate (q_{\max}) and flame temperature (T_f) at different times during the airside millimeter-size-vortex/flame interaction process.

Katta et al.

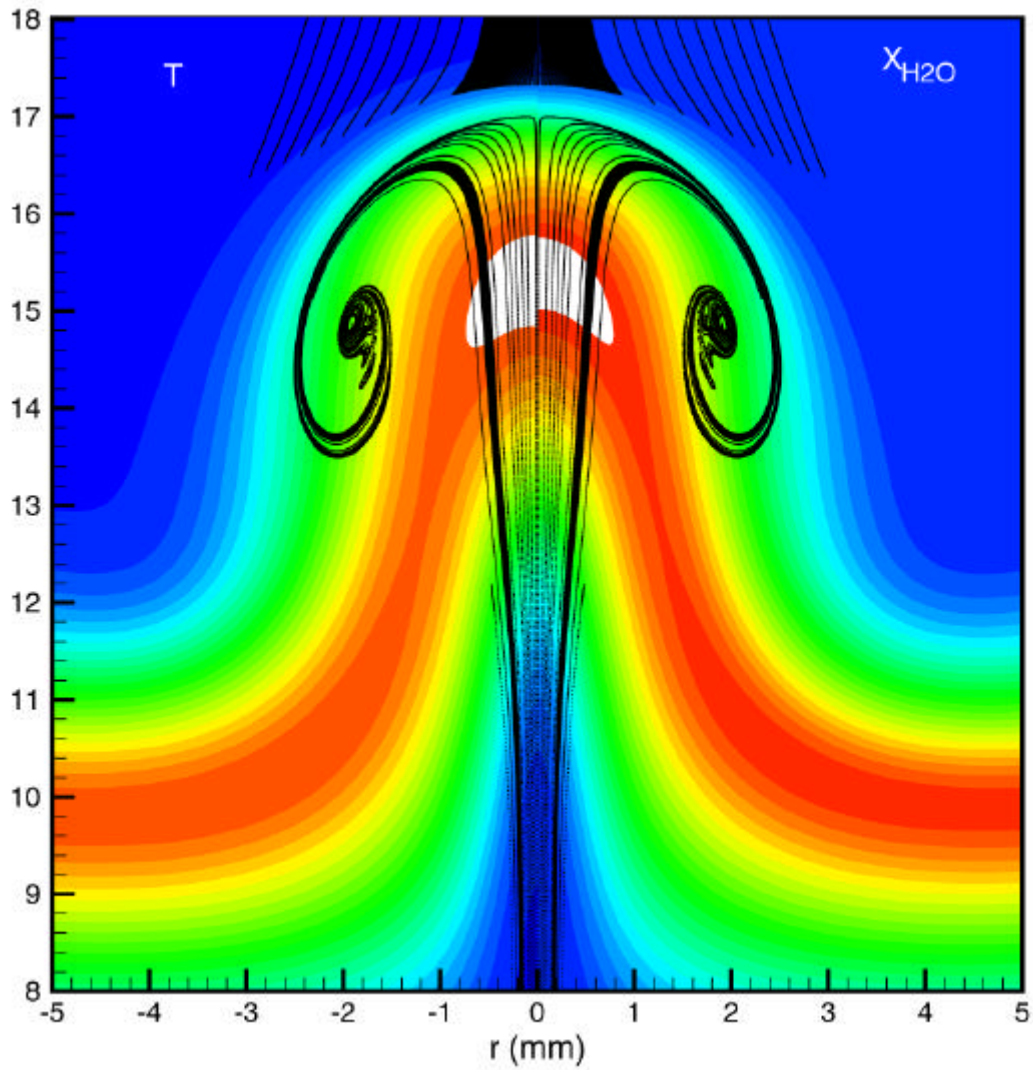


Fig. 9. Structure of the flame computed using unity-Lewis-number assumption during its interaction with a millimeter-size airside vortex. Temperature ($T_{\max} = 1410$ K) and H_2O concentration ($X_{H_2O}|_{\max} = 16.2\%$) are plotted on the left and right halves, respectively. Regions where temperature is in excess of 1410 K are shown in white color. The instantaneous locations of the particles injected from both air and fuel nozzles are superimposed.

Katta et al.

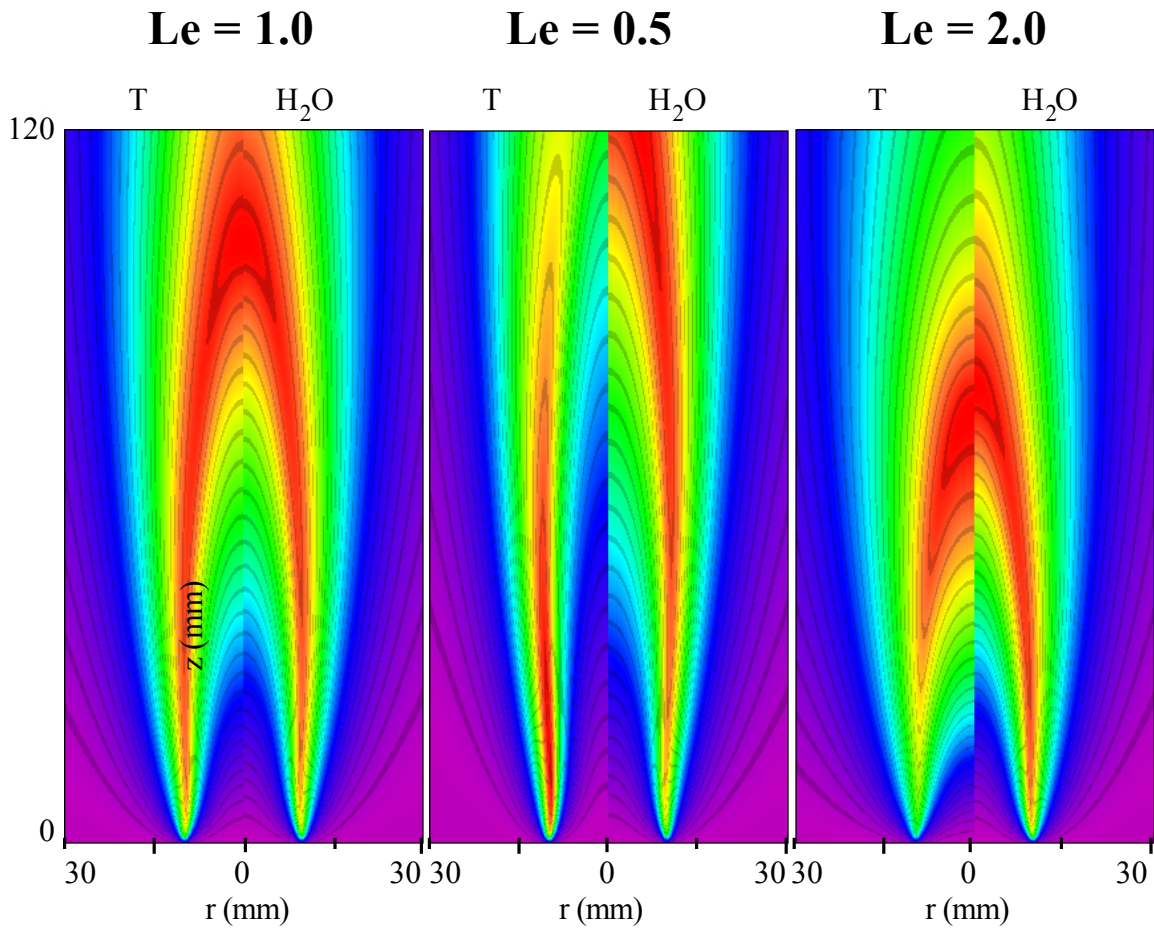


Fig. 10. Steady state flames calculated using different Lewis-number assumptions. Fuel (H₂) jet is located at the center (i.e., inside the flame). Temperature and H₂O concentration are plotted on the left and right halves, respectively, in each case.

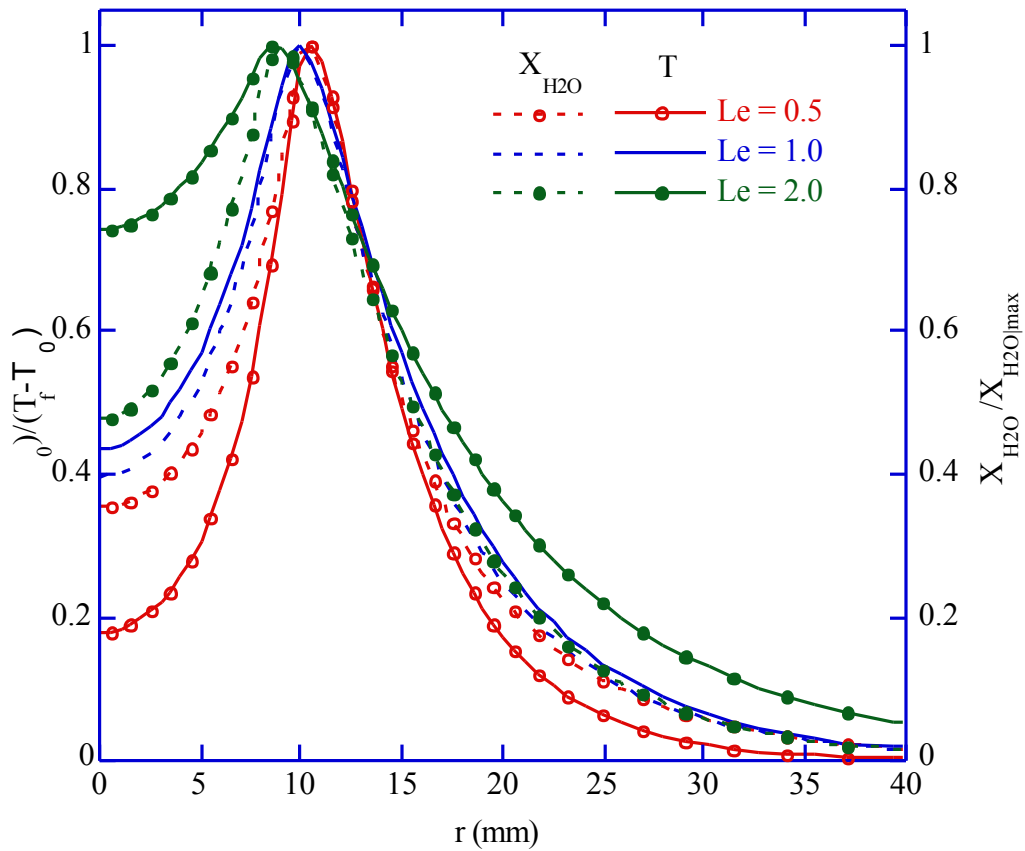


Fig. 11. Normalized temperature and H₂O distributions across the flame at an axial height of 50 mm above the inlet for flames obtained with different Lewis-number assumptions.